Multiphysics Process Simulation of the Electromagnetic-Supported Laser Beam Welding

M. Bachmann[*], V. Avilov, A. Gumenyuk and M. Rethmeier
BAM Federal Institute for Materials Research and Testing, Berlin, Germany
*Corresponding author: Unter den Eichen 87, 12205 Berlin, marcel.bachmann@bam.de

Abstract: A three-dimensional laminar steady state numerical model was used to investigate the influence of an alternating current (ac) magnetic field during high power laser beam keyhole welding of 20 mm thick non-ferromagnetic aluminum. COMSOL Multiphysics was used to calculate the three-dimensional heat transfer, fluid dynamics and electromagnetic field equations. Most important physical effects of the process were taken into account: Thermo-capillary (Marangoni) convection at the upper and lower weld pool boundaries, natural convection due to gravity and latent heat of solid-liquid phase transition. It is shown that the gravity drop-out associated with welding of thick plates due to the hydrostatic pressure can be prevented by the application of an ac magnetic field. The application of an oscillating magnetic field of 70 mT was investigated to allow for single-pass laser beam welding of thick aluminum plates. The flow pattern in the molten zone and the temperature distributions are significantly changed.

Keywords: electromagnetic weld pool support, laser beam welding, Lorentz force, Marangoni stresses, natural convection

1. Introduction

In recent years, laser deep penetration welding became a widely applied tool in industrial applications due to the available laser power of 20 kW and above for the single-pass welding of steel plates of up to 20 mm [1, 2]. In contrast to the electron beam welding, primary the evolution of the modern laser sources allowed for an electromagnetic manipulation of the hydrodynamics in the pool of liquid metal. Using high power laser beams enables for the so-called keyhole-mode welding where a small amount of the metal vaporizes and builds a vertical cavity in the plate. The surrounding liquid metal is accelerated at the surface of the weld pool due to the thermo-capillary convection [3, 4]. When welding in the single-pass technique, liquid metal tends to drop out of the weld bead due to the hydrostatic pressure p_h
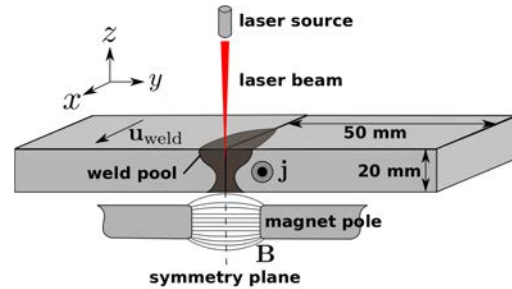

Figure 1. Simulation set-up - the laser source is located on the upper side of the specimen in the flat position.

$$p_h(z) = \rho g(h - z),$$

which, above a critical limit, cannot be balanced by the surface tension forces. Here, z, ρ, h are the vertical coordinate, the mass density and the plate thickness, respectively.

An alternating current electromagnetic system for the compensation of the hydrostatic pressure by induced Lorentz forces in the melt is numerically investigated at the single-pass full-penetration welding process of a 20 mm aluminum plate, see Figure 1.

The numerical part consists of a CFD simulation coupled with electromagnetic fields offering insights into the electromagnetically-supported welding process. Published work in the field of computational laser beam welding research can be found in [5] - [7], e.g. In general, magneto-hydrodynamics (MHD) describes the fluid flow of an electrically conducting media in presence of an electromagnetic field [8]. Theoretical principles of the working mechanisms of conducting fluids under electromagnetic conditions can be found in [9]. Electromagnetic-assisted laser beam welding experiments using high-frequency alternating magnetic fields as investigated in this paper can also be found in the literature (cf. [10, 11]).

The oscillating magnetic field induces eddy currents in the melt within the penetration depth of the material. Furthermore, the movement of the liquid conducting metal in the weld pool causes another contribution to

the currents. Lorentz forces built due to the interaction of the magnetic field and the electric current. The stabilization of the fluid flow behavior and the compensation of the hydrostatic pressure are reached by Lorentz forces in the weld pool. When the magnet is located below the specimen, these are mainly directed upwards in the molten pool (following right-hand rule) counteracting gravity. The applied oscillation frequency of the magnetic field of 450 Hz as well as the magnetic flux density of 70 mT (RMS) necessary for a complete compensation of the hydrostatic pressure were taken from preliminary experiments.

2. Numerical Modeling

The numerical modeling with COMSOL Multiphysics was done using the Non-Isothermal Flow Interface (NITF) for the calculation of the flow and the temperature field as well as the Magnetic and Electric Fields Interface (MEF) for the calculation of the electro-dynamic field quantities. The geometry and meshing of the computational domain can be seen in Figure 2.

Exploiting half symmetry along the plane that is spanned by the welding direction and the vertical axis, the weld specimen has the dimensions 115 mm x 50 mm x 20 mm.

Solving the coupled problem in segregated groups and using a multi-grid approach, the number of degrees of freedom for the coupled simulation could be limited to around 4.8 millions for the 2.15 millions linear finite elements. In Figure 3, note the visualization of the physical coupling and the corresponding coupling variables between the single physics.
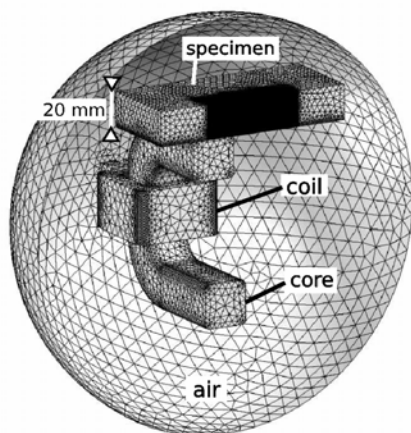

Figure 2. Geometry and fixed grid meshing of the computational domain. The magnet system (coil and core) are located below the weld specimen.
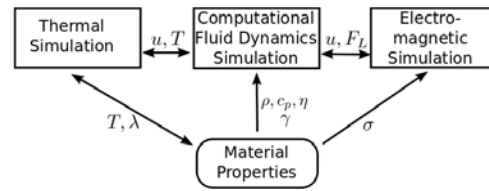

Figure 3. Physical coupling and corresponding coupling variables.
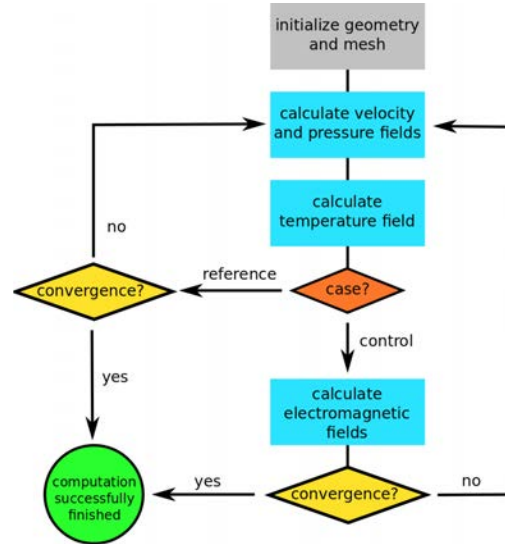

Figure 4. Simulation flowchart of the multiphysics calculation.

Here, $u, T, F_L, \lambda, \rho, c_p, \eta, \gamma, \sigma$ are the flow velocity, Lorentz force, thermal conductivity, mass density, heat capacity, dynamic viscosity, surface tension and electric conductivity, respectively. Arrows with one end denote a one-way coupling whereas arrows with two ends indicate a bi-directional coupling.

Using a segregated solver in the solution process adds the need for inner and outer loops to iterate. The convergence criterion was set to 0.001 in the solution process. For the hydrodynamic and energy equations, a stationary solution was found. The harmonic electromagnetic sub-problem was calculated using a frequency solver. The flowchart of the multi-physics simulation can be seen in Figure 4.

2.1 Assumptions

To be able to numerically handle the simulation model, it was necessary to simplify the problem to the most important physical aspects. Therefore, Marangoni convection due to the temperature-dependence of surface tension, natural convection due to gravity, and solid-liquid phase change modeling including

Table 1. Material properties taken from [13, 14]

Material property	Symbol	Value	Unit
Melting temperature	T_{melt}	933	K
Evaporation temperature	T_{evap}	2700	K
Mass density	ρ	2380	kg m^{-3}
Heat capacity	C_p^{eff}	1180	J kg^{-1} K^{-1}
Latent heat of fusion	H_f	$3.97 \cdot 10^5$	J kg^{-1}
Thermal conductivity	λ	91	W m^{-1} K^{-1}
Dynamic viscosity	η	$1.1 \cdot 10^{-3}$	Pa s
Marangoni coefficient	$\partial\gamma/\partial T$	$-1.55 \cdot 10^{-4}$	N m^{-1} K^{-1}
Electrical resistivity	$\rho_{el} = \sigma^{-1}$	$24.77 \cdot 10^{-8}$	Ω m

latent heat of fusion as well as the harmonic excitation of the magnetic field were included.

Further assumptions for the simulation were as follows:

- Steady state simulation.
- Fixed keyhole and weld pool surfaces.
- Laminar flow pattern.
- Time-averaged Lorentz force over one oscillation period serves as an input volume force to the hydrodynamic part of the simulation.
- The solid-liquid phase change behaviour is calculated by an additional source term that dampens the velocity in the solid phase to the processing speed [12] using a solidification range.
- Inductive heating of the work-piece caused by the electric currents is not accounted for due to the strong heating of the laser source up to evaporation temperature of the material.

The thermo-physical properties for the numerical simulations were taken from [13, 14]. They are summarized in Figure 5 and Table 1.

2.2 Governing Equations

In this paragraph, the governing equations for the mass conservation, momentum and energy transport are presented as they are implemented in COMSOL:

- Mass Conservation
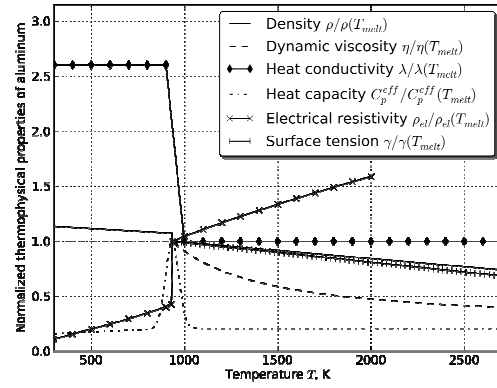
$$\nabla \cdot (\rho\boldsymbol{u}) = 0$$

Figure 5. Thermo-physical properties for pure aluminum taken from [13, 14].

- Momentum equation

$$\rho(\boldsymbol{u} \cdot \nabla)\boldsymbol{u} = -\nabla p + \nabla \cdot \left(\eta\left(\nabla\boldsymbol{u} + (\nabla\boldsymbol{u})^T\right) - \frac{2}{3}\eta(\nabla \cdot \boldsymbol{u})\boldsymbol{I} \right) + \boldsymbol{F}$$

The source F term holds the gravitational forces, the model for the solidification behavior as well as the electromagnetic force:

$$\boldsymbol{F} = -\rho\boldsymbol{g} - c_1 \frac{(1 - f_L)^2}{f_L^{~3} + \varepsilon}(\boldsymbol{u} - \boldsymbol{u}_{weld}) + \langle \boldsymbol{j} \times \boldsymbol{B} \rangle$$

Here, c_1 and ε are computational constants and f_L denotes the liquid fraction which varies from 0 to 1 between the solidus and liquidus temperature.

$$f_L = \begin{cases} 0 & T < T_{sol} \\ \dfrac{T - T_{sol}}{T_{sol} - T_{liq}} & T_{sol} \le T \le T_{liq} \\ 1 & T > T_{liq} \end{cases}.$$
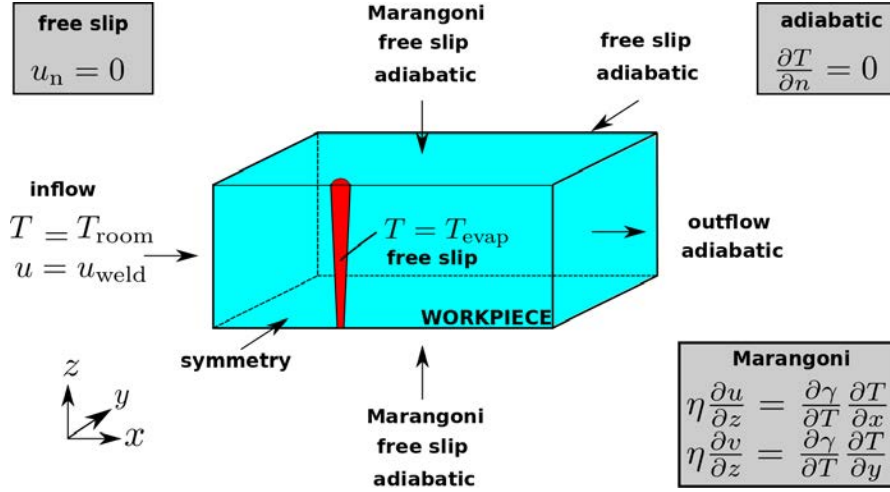
Figure 6. CFD boundary conditions.

- Energy conservation

$$\rho C_p^{eff} \boldsymbol{u} \cdot \nabla T = \nabla \cdot (\lambda \nabla T)$$

C_p^{eff} denotes an effective heat capacity formulation. The latent heat amount H_f is normalized around the melting temperature within a temperature range δT of 50 K

$$C_p^{eff} = C_p^0 + \frac{\exp\left[\left(\frac{T - T_{melt}}{\delta T}\right)^2\right]}{\sqrt{\pi}\delta T} H_f.$$

The Maxwell equations are valid in quasi-stationary form for the magnetic field $\boldsymbol{B}$ and the electric field $\boldsymbol{E}$ as follows:

$$\nabla \times \boldsymbol{B} = \mu_0 \boldsymbol{j},$$
$$\nabla \times \boldsymbol{E} = -\frac{\partial \boldsymbol{B}}{\partial t}.$$

μ_0 is the magnetic permeability of vacuum and $\boldsymbol{j}$ is the electric current density and reads

$$\boldsymbol{j} = \sigma(\boldsymbol{E} + \boldsymbol{u} \times \boldsymbol{B}).$$

The second term is due to the movement of electrically conducting media (liquid metal) perpendicular to the magnetic field.

To effectively compensate for the hydrostatic pressure, the magnetic field penetration must be around half the penetration depth of the laser. For the investigated case of full penetration welding of a 20 mm thick aluminum specimen, a frequency of 450 Hz was chosen leading to a skin depth δ of around 11 mm in the liquid metal. The skin depth for the electromagnetic field reads as follows [8]:

$$\delta = (\pi f \mu_0 \sigma)^{-0.5},$$

where f is the frequency and σ is the electric conductivity. The frequencies of potentially unstable surface waves are of lower order of magnitude than the oscillation frequency of the magnetic field. Therefore, the time-averaged Lorentz force contribution was used as source term for the fluid dynamic simulation and the oscillating part of the Lorentz force was neglected. The applied Lorentz force is mainly directed upwards in the melt (the magnet system was below the specimen) counteracting gravitational forces. The potential part of the Lorentz force distribution acts as a magnetic pressure p_{EM} on the flow field which is proportional to the effective value of the applied magnetic flux density squared

$$p_{EM} = \int_z \langle F_L^z \rangle dz \propto \frac{B_{rms}^2}{2\mu_0}.$$

2.3 Boundary Conditions

The boundary conditions for the fluid flow simulation coupled with heat transfer in the weld specimen can be seen in Figure 6. Note the Marangoni boundary conditions on the upper and lower surface of the plate due to the temperature-dependant surface tension. For pure metals, the temperature-derivative of the surface tension is negative leading to a flow component near the surface from hot to colder regions. The keyhole geometry is a right-

circular cone with radius 0.4 mm at the upper side and 0.2 mm at the root side. The fixed keyhole surface is set to evaporation temperature. The process velocity for the welding was set to 0.5 m min^{-1}. This value was experimentally determined to obtain full-penetration welding at 20 mm aluminum alloy plates at 15 kW laser power

For the electromagnetic part of the simulation, the coil ends (see Figure 2) were excited by a voltage difference. At the outer air boundary the magnetic field was vanishing. The cross section of the magnet poles as well as the distance between them was 25 mm. The magnet system was located 2 mm below the weld specimen. The symmetry plane was a perfect magnetic conductor (vanishing tangential component of the magnetic field).

3. Results

This section shows the results of the stationary simulations of an aluminum plate of 20 mm thickness under reference (no magnetic field) and control conditions (oscillating magnetic field applied). The liquid metal speed and the temperature distribution for the reference case as well as the case with magnetic field applied can be seen in Figure 7.

3.1 Reference case without electromagnetic forces

In this configuration the flow behavior is strongly determined by the action of the Marangoni forces on the upper as well as the lower weld pool surfaces. Note the strong
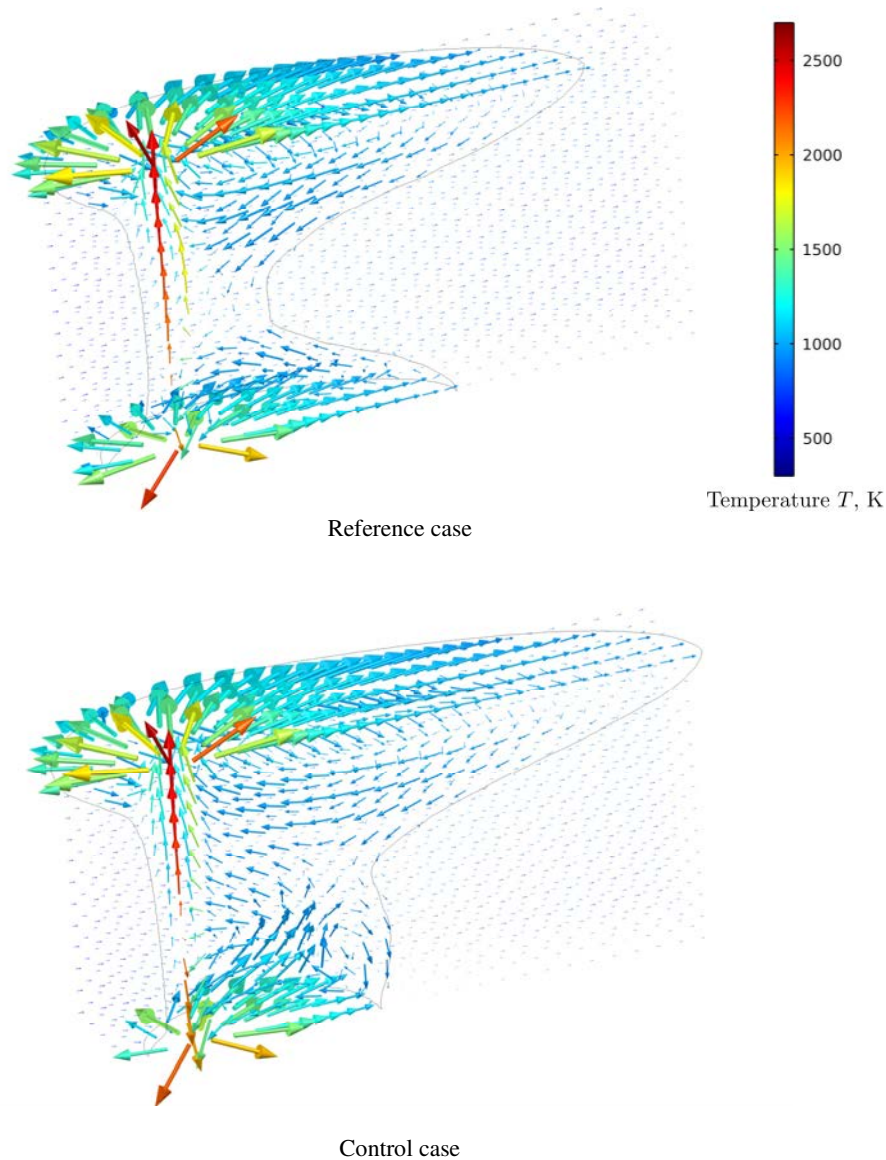

Reference case

Control case

Figure 7. Velocity field into the molten pool for the reference case without electromagnetic forces applied (upper picture) and the control case with B_{RMS}=70 mT (lower picture). The colors refer to the temperature.
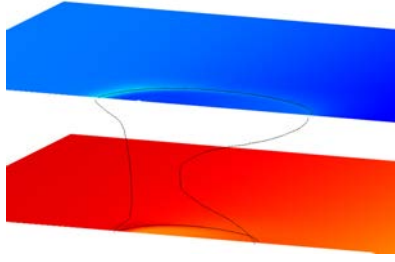
Figure 8. Pressure distributions on the upper and the lower surface of the plate for the reference case. The pressure difference between both sides is due to the hydrostatic pressure.
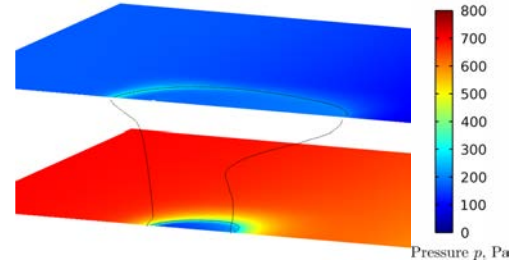

Figure 9. Pressure distributions with oscillating magnetic field applied. The pressure difference between both sides due to the hydrostatic pressure is compensated by the applied Lorentz forces.

three-dimensional vortex structures that form beginning at the keyhole endings and spanning up to the solid-liquid interfaces of the weld pool. Below the surfaces, the flow returns to the keyhole vicinity obeying the mass conservation law. Near the keyhole the flow is directed upwards due to the natural convection that results from the impact of gravity and mass density variations according to the applied evaporation temperature at the keyhole surface. The occurring flow velocities are up to 40 times higher than the processing speed of the laser beam welding.

Experimental observations show that the liquid metal drops out at the root side of the weld in this configuration, because the surface tension forces cannot balance the large hydrostatic pressure, note Figure 8. Therefore, a successful welding process is impossible in this configuration without any kind of weld pool support.

3.2 Control case with B_{RMS}=70 mT

The results of the process simulation with the proposed inductive electromagnetic weld pool support system applied are presented in Figure 7. Within the penetration depth of the applied Lorentz forces, the flow is accelerated in vertical direction leading to a larger influence of the Marangoni flow into the depth of the material. In contrast, the weld pool extents parallel to the welding direction are reduced. An additional vortex structure builds up at the lower rear weld pool side which is directed against the existing Marangoni vortex.

Table 2. Averaged pressure differences between the upper and lower weld pool surfaces

	Averaged pressure difference
Reference case	460 Pa
Control case	12 Pa

The upper side of the weld pool looks similar to the reference case due to the limited penetration depth of the magnetic field and the corresponding Lorentz forces. Solely the enhanced vertical heat exchange by the induced flow leads to a slightly elongated weld bead.

The pressure on the lower and upper weld pool surfaces are presented in Figure 9. Note the pressure within the liquid phase on the lower weld pool side which is of the same order of magnitude like on the upper side due to the compensation of the hydrostatic pressure by the electromagnetic forces. The pressure values in regions with temperatures below the melting point of the material have no relevance for the realistic welding process as solid state is present there. They result from modeling the whole plate (solid and liquid region) as a single-phase fluid. Numerically, both phases differ only in their temperature-dependent material properties and braking forces in the solid region to ensure processing velocity there in the simulations. The averaged pressure differences (see Table 2) between upper and lower weld pool surface in the liquid region give rise to the successful application of the inductive weld pool support system.

Another aspect is the electromagnetically induced drag. This can be expressed in terms of the dimensionless Hartmann number

$$Ha^2 = (B^{RMS} L)^2 \frac{\sigma}{\eta},$$

where L is the half weld pool width on the side where the magnet system was located. As a result from the simulations, the maximum Hartmann number was around 300. That and the enhanced vertical momentum give reasons for the smaller weld bead dimensions on weld root side.

4. Conclusions

The application of a harmonic magnetic field on the laser beam welding process of a 20 mm thick aluminum plate was numerically investigated. The liquid metal velocity, pressure, temperature and electromagnetic field quantities were calculated.

It was shown, that the application of an oscillating magnetic field and its induced eddy currents result in a Lorentz force in the weld specimen that acts as a magnetic pressure. At an oscillation frequency of 450 Hz and a magnetic flux density of B_{RMS}=70 mT, the magnetic support system was capable to successfully compensate for the hydrostatic pressure of the column of liquid aluminum in the weld bead above the magnet system. The magnetically induced drag component and the resulting flow pattern lower the influence of the Marangoni stresses at the root side of the specimen within the penetration depth of the applied fields.

5. References

1. F Vollertsen, S Grünenwald et al., Welding thick steel plates using fibre lasers and GMAW, *Weld. World,* **54**, R62 – R70 (2010)
2. M Rethmeier, S Gook et al., Laser-Hybrid Welding of Thick Plates up to 32 mm using a 20 kW Fibre Laser, *Japan Welding Society*, **27**, 74s – 79s (2009)
3. J F Ready and D F Farson, *LIA Handbook of Laser Materials Processing*, Springer, Berlin (2001)
4. J Dowden, *The Theory of Laser Materials Processing: Heat and Mass Transfer in Modern Technology*, Springer, Netherlands (2009)
5. T Fuhrich, P Berger et al., Marangoni effect in laser deep penetration welding of steel, *J. Laser Appl.*, **13**, 178 – 86 (2001)
6. A Mahrle and J Schmidt, The influence of fluid flow phenomena on the laser beam welding process, *Int. J. Heat Fluid Fl.*, **23**, 288 – 97 (2002)
7. B Ribic, R Rai et al., Numerical simulation of heat transfer and fluid flow in GTA/laser hybrid welding, *Sci. Technol. Weld. Joi.*, **13**, 683 – 93 (2008)
8. R Moreau, *Magnetohydrodynamics*, Kluwer Academic Publishers (1990)
9. V Bojarevics, J A Freibergs et al., *Electrically induced vertical flows*, Kluwer London (1989)
10. V V Avilov, R Moldovan et al., Electromagnetic weld pool control system for laser beam welding of thick metal plates, *Proceedings of the IWOTE08*, BIAS Verlag Bremen, 413 – 20 (2008)
11. V V Avilov, R Moldovan, Electromagnetic weld pool control by CO2 and YAG disk laser welding of thick stainless steel plates, *Proceedings of EPM 2009*, Dresden, Germany (2009)
12. A D Brent, V R Voller and K J Reid, Enthalpy-porosity technique for modelling convection-diffusion phase change: application to the melting of pure metal, *Numer. Heat Transfer*, **13,** 297 – 318 (1998)
13. K C Mills, *Recommended Values of Thermophysical Properties for Selected Commercial Alloys*, Woodhead Publishing Ltd. (2002)
14. B J Keene, Review of data for the surface tension of pure metals, *Int. Mater. Rev.*, **38**, 157 – 92 (1993)